


Article

Aerodynamic Performance and Coupling Gain Effect of Archimedes Spiral Wind Turbine Array

Ke Song¹ , Huiting Huan², Liuchuang Wei¹ and Chunxia Liu^{3,*}

¹ School of Mechanical and Electrical Engineering, Kunming University, Kunming 650214, China; songke@kmu.edu.cn (K.S.); weiliuchuang@126.com (L.W.)

² School of Mechano-Electronic Engineering, Xidian University, Xi'an 710071, China; hthuan@xidian.edu.cn

³ School of Statistic and Mathematics, Yunnan University of Finance and Economics, Kunming 650221, China

* Correspondence: lcx13099971218@163.com

Abstract: The Archimedes spiral wind turbine (ASWT), as a novel type of horizontal-axis wind turbine, is well suited for remote islands. To explore the aerodynamic performance and coupling gain effect of ASWT array, a three-dimensional numerical simulation was carried out using the computational fluid dynamics (CFD) method. The influence of arrangement, relative spacing, and rotation configuration on the performance of a double-unit array and triangular array is studied. The results demonstrate that, in parallel arrangements, the double unit achieve higher performance than an isolated ASWT within a specific range of parallel spacing. However, the effect of performance improvement gradually diminishes as the parallel spacing increases. In tandem arrangements, the upstream unit performance remains largely unaffected when tandem spacing exceeds 5 D, while the downstream unit's performance declines notably with reducing tandem spacing. The downstream unit in reverse rotation configuration accrues more energy than its counterpart operating at the co-rotation configuration. In triangular arrangements, the reverse rotation configuration can achieve better performance due to the meshing effect between the wake of the upstream ASWT and the downstream ASWT. This configuration allows the array system to maintain a higher maximum power output within a smaller spacing. The research results can provide a basis and reference for designing the layout scheme of a multi-unit ASWT power station.

Keywords: Archimedes spiral wind turbine; array; aerodynamic performance; coupling gain effect



Citation: Song, K.; Huan, H.; Wei, L.; Liu, C. Aerodynamic Performance and Coupling Gain Effect of Archimedes Spiral Wind Turbine Array. *J. Mar. Sci. Eng.* **2024**, *12*, 1062. <https://doi.org/10.3390/jmse12071062>

Academic Editors: Martin Otto Laver Hansen and Galih Bangsa

Received: 2 May 2024

Revised: 3 June 2024

Accepted: 8 June 2024

Published: 24 June 2024



Copyright: © 2024 by the authors. Licensee MDPI, Basel, Switzerland. This article is an open access article distributed under the terms and conditions of the Creative Commons Attribution (CC BY) license (<https://creativecommons.org/licenses/by/4.0/>).

1. Introduction

Across the globe, thousands of remote islands are inhabited, serving crucial purposes like territorial protection, local development, and the preservation of culture and the environment. Consequently, the management of these islands holds substantial diplomatic and economic implications. With the growing importance of border islands in light of geopolitical concerns like territorial waters and marine resources, subsidies for both inhabited and uninhabited islands have risen. This increased support extends to designated remote islands, where promoting economic and social independence is vital for fostering sustainable and prosperous communities, particularly in border areas. Given the limited access to traditional energy sources like fossil fuels on remote islands, renewable energy plays a pivotal role in establishing resilient island societies. However, challenges of social, economic, and local nature have impeded the widespread adoption of renewable energy [1,2]. Most border islands are geographically isolated from the mainland, making submarine electricity grid connections economically unfeasible. As a result, small local thermal power plants that use internal combustion for electricity generation remain the primary energy source for remote islands without grid connections. Despite the significant cost implications, typically three to five times higher than mainland prices, a universal service pricing model ensures that residents pay similar electricity rates, with the variation subsidized by all electricity consumers. The issue of high electricity costs on remote

islands is not only a local concern but also a national and regional priority, necessitating a shift to alternative energy systems that strike a balance between economic viability and environmental sustainability [3]. Wind energy has emerged as a compelling alternative to fossil fuels, thanks to its abundant resources and straightforward development processes, attracting growing interest among various renewable energy options [4]. The evolution of wind turbine technology has been rapid, playing a crucial role in the advancement of wind energy technologies and providing a practical alternative for electricity generation in remote islands [5].

Although wind turbine technologies have advanced significantly, practical challenges remain when deploying them on remote islands. Typical commercial wind turbines [6,7] are lift-type [8], designed to operate optimally at high wind speeds (over 6 m/s) [9,10] in mainland or offshore wind farms to maximize power generation. These turbines are frequently installed in areas with the highest local wind flow, whereas certain remote islands typically encounter low wind speeds. As a result, they will have limited self-starting capabilities, low output efficiency, or zero output power issues, requiring additional auxiliary start-up devices like pitch control systems and auxiliary motors. Given the limited conditions on remote islands, the installation and troubleshooting of conventional commercial wind turbines at these locations present substantial challenges and expenses, posing a hurdle to the effective utilization of wind energy [11,12]. Therefore, the development of a novel type of wind turbine capable of self-starting under low wind flow conditions is pivotal for the advancement of remote islands in power generation systems. One promising solution is the Archimedes Spiral Wind Turbine (ASWT). This innovative turbine (a small type of wind turbine), designed on the principles of the Archimedean spiral, primarily utilizes drag forces, operates at a lower cutting speed and is easy to deploy compared to various other types of wind turbines [13]. In our previous study, we have conducted aerodynamic performance and output power analysis on ASWT with different blade angles, and the results show that they are all suitable for operation under low wind speed and low tip speed ratio conditions [14]. Consequently, the installation of an appropriate ASWT at remote islands, without necessitating alterations to their ecological environment, resonates strongly with the ethos of remote islands low-carbon development.

Recently, in the realm of assessing the power performance of ASWT, various researchers have employed a combination of theoretical models, computational fluid dynamics (CFD) tools, and practical experimentation. Lu et al. [15] delved into this domain by utilizing a theoretical model alongside a CFD tool to scrutinize the power output of ASWTs. Building upon this foundation, Kim et al. [16] conducted an extensive three-dimensional analysis, merging theoretical frameworks with practical insights garnered from PIV measurements and CFD simulations. Further investigations by Safidari et al. [17] extended the understanding through a comprehensive CFD analysis complemented by experimental validation to assess the output performance of ASWTs. Expanding on the practical implications, Chaudhary et al. [18] highlighted the suitability of ASWTs for low-wind locales, emphasizing their minimum cut-off speed of approximately 2.5 m/s. Blade design emerged as a focal point in subsequent studies. Rao et al. [19] explored the impact of blade aerofoil configurations on ASWT output, while Jang et al. [20] conducted experimental tests across varying wind speeds to glean insights into overall performance. Nawar et al. [21] delved into the nuances of blade angles and aerodynamic performance through CFD analysis and empirical experimentation, respectively. The multifaceted nature of ASWT optimization is further underscored by Kamal et al. [22,23], who investigated the interplay of blade thickness, aerofoil shape, and blade angle on turbine efficiency. Additionally, Al-murshedi [24] contributed to the discourse with a simulation study that scrutinized the impact of both static and dynamic loading conditions on ASWTs. Lastly, Refaie et al. [25,26] pursued avenues for efficiency enhancement through the implementation of wind shrouds, employing numerical simulations to validate their findings.

After conducting a comprehensive analysis of previous research, various steps were taken to improve the power generation of ASWT. These steps involved making adjustments

to the design features of the turbine blades and incorporating a shroud into the turbine. To facilitate ease and simplicity, the findings of multiple research advancements related to ASWT (including current work) have been summarized in Table 1. Additionally, it should be noted that wind turbines are often arranged in arrays to increase the energy density in practical applications [27,28]. However, wind turbines of the lift-type are sensitive to the wake disturbances generated by adjacent turbines. Tang et al. [29] conducted wind tunnel tests to study the wake characteristics of a horizontal-axis wind turbine and the impact of the wake on the performance of a downstream turbine. They found that the upstream turbine caused smaller disturbances to the flow. However, as the blade rotation speed increased, larger changes in velocity and turbulence intensity occurred in the wake. The loss in output power of the downstream turbine largely depended on the wake characteristics of the upstream turbine. For arrays of lift-type hydrokinetic turbines, optimizing both the energy density of the turbine farm and the performance of each individual turbine presents conflicting objectives. However, due to its substantial solidity, the ASWT generally has a lower optimal tip speed ratio compared to lift-type wind turbines. This leads to comparatively minimal interference between adjacent turbines in ASWT arrays, allowing for denser packing and higher energy density. At the same time, the individual turbine performance is maintained through accelerated bypass flow [30]. However, there are no research studies until now dealing the aerodynamic interactions of ASWTs. Therefore, the presented study is supposed to be an achievement in its field to outline and investigate the consistent attributes of coupling gain effects on ASWT array using a CFD approach, with a focus on three key aspects: arrangement, relative spacing, and rotation configuration. The structure of this work is as follows: Section 2 presents the governing equations and aerodynamic coefficients, along with the numerical setup and validation. Section 3 discusses the results for the parallel arrangement, tandem arrangement, and triangular array. Finally, Section 4 offers a conclusion summarizing the key findings of this study.

Table 1. Important research progresses for ASWT.

Progress	Description	Outcome
Kim et al. [15]	A theoretical and practical analysis on ASWT	Addressing a theoretical approach to design the turbine.
Labib et al. [31]	The effect of aspect ratio was analyzed.	The maximum power coefficient was increased to 0.249 by extending the aspect ratio at a tip-speed ratio of 1.413.
Rao et al. [19]	Add an aerofoil to the blade of ASWT.	The aerofoiled turbine significantly increased the torque when compared to the original turbine.
Nawar et al. [21]	Variable-angle rotors were analyzed.	The variable-angle rotor’s output power increased by 14.7% in comparison to the fixed-angle rotor.
Refaie et al. [25]	Add a shroud to ASWT	The shrouded ASWT demonstrated a 2.1 times improvement in power compared to the bare rotor.
Kamal et al. [22]	The thickness of the blades affecting the performance was analyzed.	Performance is enhanced by reducing rotor blade thickness.
Current work	Aerodynamic performance and coupling gain effect of ASWT array were analyzed.	The reverse rotation configuration in parallel arrangement achieves the maximum coupling gain at a spacing of 1.1 D. The triangular array can achieve a 2.56% increase in the maximum performance under an optimal configuration.

2. Numerical Methods

The ASWT’s aerodynamic performance is estimated in terms of power coefficient (C_P), thrust coefficient (C_T), and tip speed ratio (TSR). Power coefficient is defined as the ratio of power produced by a turbine to the available power in the wind as follows:

$$C_P = \frac{P}{0.5\rho AV_0^3} \tag{1}$$

Thrust coefficient is defined by:

$$C_T = \frac{T}{0.5\rho AV_0^2} \tag{2}$$

The tip speed ratio is defined by:

$$TSR = \frac{\omega R}{V_0} = \frac{\pi n R}{30 V_0} \tag{3}$$

where P represents the power output (W), T represents the turbine thrust (N), V_0 represents the incoming wind velocity (m/s), n represents the turbine angular velocity (rpm), A represents the area of a reference surface (m²), and R is the radius of turbine (m).

2.1. Geometry of the ASWT

The ASWT comprises a cylinder shaft which houses three blades, each blade possessing a radius of 125 mm, positioned at a 120° angle. The specified radius of the ASWT is defined as the vertical separation between the blade tip at its exit and the axis. Figure 1 illustrates a schematic representation of the ASWT. Further geometry details can be found in the previous study of 30-45-60 ASWT [14]. Figure 1 provides a schematic representation of the ASWT.

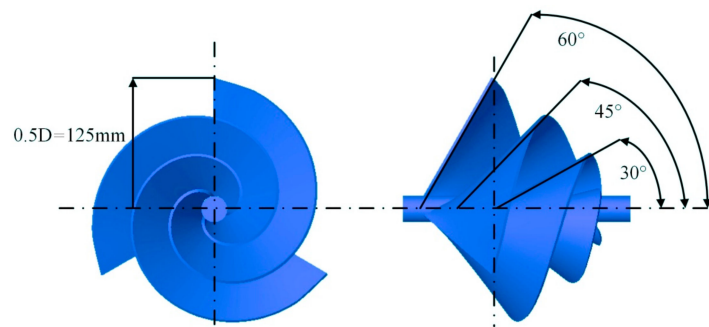


Figure 1. Schematic view of the ASWT.

2.2. Simulation Setup

The finite-volume commercial software ANSYS Fluent 17.1 software (Ansys Inc., Canonsburg, Washington, PA, USA) was used to solve the 3D Reynolds-averaged Navier–Stokes (RANS) equations coupled with the SST $k - \omega$ turbulence model [32] for accurate closure. This model is capable of modeling the transport of turbulent shear stress, providing accurate predictions on the onset and amount of flow separation under adverse pressure gradients. It has been widely used in the CFD simulation of wind turbines. The pressure–velocity coupling was implemented using the SIMPLE algorithm. To manage the convective and viscous terms in the governing equations, second-order upwind schemes were utilized for discretization. Additionally, second-order interpolation with central differencing was employed for pressure computations. Figure 2 displays the two calculation domains for parallel arrangement and tandem arrangement, which comprises two stationary domains and a rotatory domain (x is parallel spacing, and z is tandem spacing). The ASWT rotor is located in the rotatory domain, while the stationary domain is exposed to the incoming wind. To define the rotation of the rotor relative to the stationary domain, the rotatory domain was set as a cylinder, ensuring a relative slip between the interfaces and the flow field information transmission. The rotatory domain’s dimensions were slightly larger than the rotor shaft and diameter. At the velocity inlet, a uniform wind speed (V_0) of 5 m/s was applied, and the outlet was set as a pressure outlet. The rotor was positioned 5 D away from the inlet and 20 D away from the outlet. The rotor was subjected to a non-slip condition, while the stationary domain’s surrounding boundary used a free-slip condition.

To ensure accurate simulation results, it is crucial to have a suitable mesh because it directly affects the accuracy of simulation results. The drawback associated with the utilization of structured grids lies in the manual and time-intensive nature of the mesh generation process [33,34]. On the contrary, unstructured grids offer a more cost-effective solution due to their automatic generation process. Nevertheless, when employing unstructured meshes, it is crucial to meticulously manage grid quality parameters, including skewness, aspect ratio, and orthogonal quality in the proximity of grid density. This precautionary measure is essential to prevent any detrimental effects on simulation accuracy [35]. In this study, an unstructured mesh was used to create the computational domain, which includes both stationary and rotatory domains. The levels of skewness, aspect ratio, and orthogonal quality fall within the range reported in other studies [36,37]. However, for simulating flow in the boundary layer, particularly near the blade surfaces, a prism grid with 10 inflation layers was employed. This approach aimed to capture the effects of adverse pressure and rapid changes on flow characteristics around the ASWT blades. In the context of turbulence models, the Y^+ parameter holds significant importance. It represents the non-dimensional distance from the non-slip wall to the first mesh node and is determined based on the employed turbulence models. Numerous studies suggest that maintaining Y^+ values of ≤ 15 is acceptable when using the SST $k - \omega$ turbulence model [38,39]. In this study, Y^+ was deliberately set to be less than 1 [40,41]. This precautionary measure is taken because higher Y^+ values would result in reduced simulation accuracy, as the wall functions prescribed by ANSYS Fluent would not effectively resolve the boundary layer flow [42]. In addition, due to the ASWT having complex geometry, the turbine surface grids were further refined. To improve the credibility of the analysis, the implementation of fine mesh regions around the blades was employed to capture the air flow behavior. Moreover, ten prism layers were created in proximity to the rotor surfaces to accurately capture the high gradient flow properties within the boundary layer region. On the other hand, to ensure the mesh independency, C_P and C_T defined in Section 2 were selected as the determining factors in the mesh independence assessment, and three different sets of mesh were utilized (shown in Table 2). The results suggest that there is little difference between the medium and fine mesh, implying that further increasing the mesh resolution would have an insignificant impact on the CFD outcomes. According to the economy of time in the simulation, the medium mesh set was selected to perform the numerical simulations for the subsequent calculations. Additionally, it should be noted that the Sugon high-performance computing system with Xeon E7 (64 cores used) was utilized for the simulation. In the present study, around 500 iterations were found to be sufficient for the isolated ASWT case numerical solution. Each case required approximately 21 core hours to complete the calculation process.

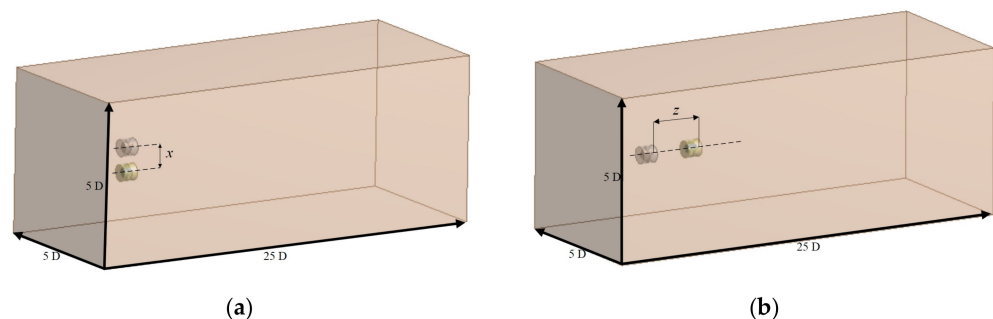


Figure 2. Calculation domain: (a) parallel arrangement DT; (b) tandem arrangement.

Table 2. Mesh independence assessment.

Mesh Density	Total Cells (Million)	C_P	C_T
Coarse	4	0.230	0.675
Medium	5	0.234	0.679
Fine	6	0.234	0.680

2.3. Validation of Numerical Simulation

To validate the current model, Figure 3 displays a comparison between the experimental data of the ASWT rotor reported by Kamal et al. [22] and the CFD results obtained using C_P . It is apparent that there is a slight deviation between the CFD and experimental data. This occurrence can be attributed to several factors that affect both the CFD simulation and experimental test, including the precision of measurement instruments, the impact of the ambient temperature fluctuations on air density, and the limitations of the turbulence model. However, overall, the CFD values are in very good agreement with the experimental data, which have verified the accuracy of the model and method adopted in current work. Additionally, the CFD results reveal that the C_P of the ASWT initially rises and then decreases as the TSR increases, mirroring the behavior observed in traditional HAWT. Within the TSR range of 1.0 to 2.0, the C_P value surpasses 0.2 and peaks at 0.234 when TSR is 1.5. Consequently, subsequent calculations for ASWT array will consistently utilize the optimal TSR of 1.5.

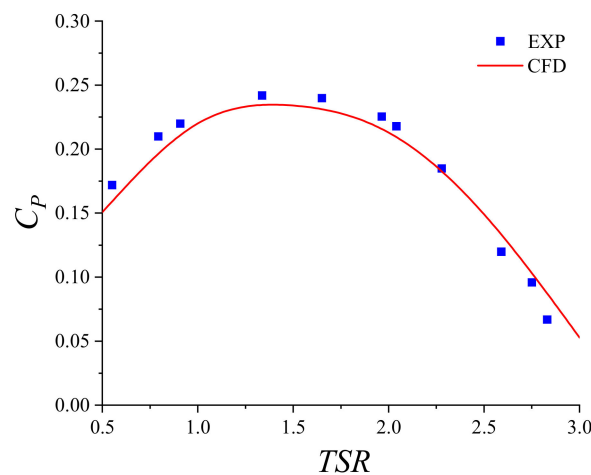


Figure 3. Comparison between the experimental value and the CFD value.

3. Results and Discussion

3.1. Parallel Arrangement

Figure 4 illustrates the variations in C_P and C_T of parallel arrangement of double units as the parallel spacing (x) changes. Due to the blocking effect, both reverse and co-rotation configurations achieve higher performance than the isolated ASWT within a specific range of parallel spacing. Furthermore, when the x is 1.1 D, the C_P and C_T of the double ASWTs reach their peaks in both the reverse and co-rotation configurations. Compared to the isolated ASWT, the C_P of the left and right units in reverse rotation configuration increased by 3.47% and 3.58%, respectively, resulting in an average increase of 3.53%. Similarly, the C_T increased by 3.26% and 3.33%, respectively, with an average increase of 3.30%. In contrast, when comparing the isolated ASWT to the left and right units in co-rotation configuration, the C_P increased by 1.58% and 2.63%, respectively, resulting in an average increase of 2.11%. Correspondingly, the C_T increased by 1.44% and 2.88%, respectively, with an average increase of 2.16%. Moreover, the C_P and C_T of the left and right units in both configurations exhibit a continuous decreasing trend as the

parallel spacing increases, eventually approaching the C_P and C_T of an isolated ASWT. When $x = 4 D$, the average C_P of the two-unit array in reverse rotation and co-rotation configurations only increased by 0.46% and 0.36%, respectively, compared to isolated ASWT, while the average C_T only increased by 0.62% and 0.57%, respectively. Therefore, the blocking effect gradually weakens as the parallel spacing increases. When x exceeds 4 D, the performance gain from the blocking effect is very small. On the other hand, it is evident that the reverse rotation configuration is more suitable for double units compared to the co-rotation configuration. While the peak C_P of both rotation configurations is similar, the average C_P of the reverse rotation configuration is higher. Moreover, when considering small spacing, the contrast in C_P and C_T between the two units in the co-rotation configuration becomes more pronounced, potentially resulting in problems such as unstable output and uneven force on the connecting support structure.

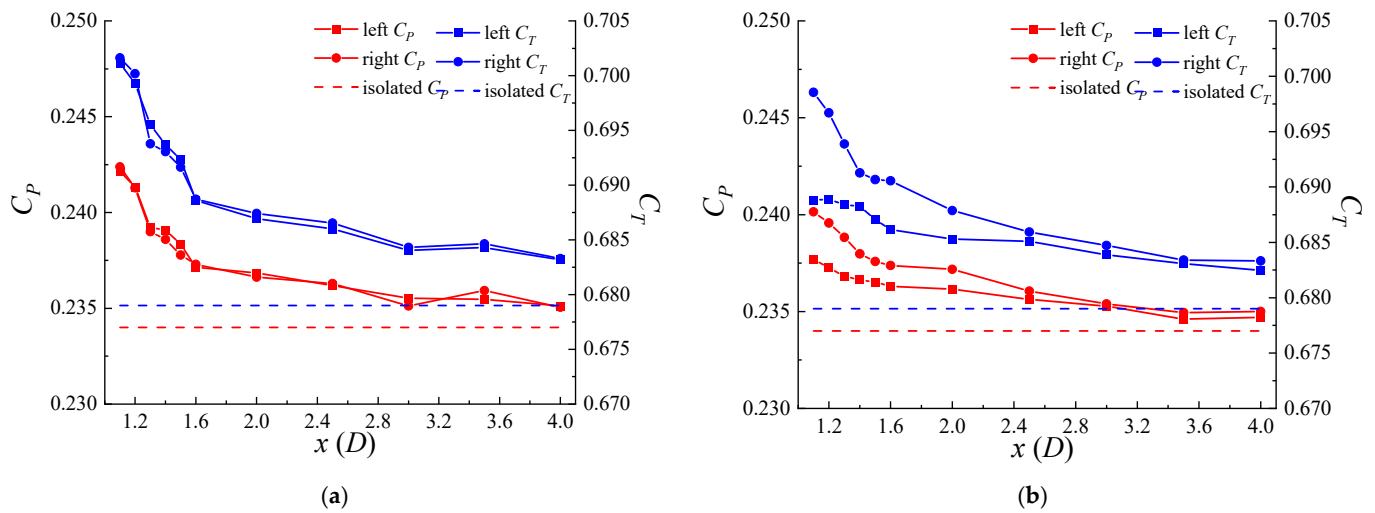


Figure 4. C_P and C_T versus x for the double units: (a) reverse rotation; (b) co-rotation.

Figure 5 illustrates the velocity contours for the double units at different x . Within a specific range of parallel spacing, as the double units approach each other, a high-speed zone emerges around them, notably amplifying the acceleration effect within the central flow channel. This is attributed to both the inherent axial length of the ASWT and the obstructive influence, resulting in sustained impact from the acceleration zone within the central flow channel on both the inflow and the sides [43,44], which is similar to the results of traditional horizontal-axis turbines. Consequently, the double units achieve higher performance than the isolated ASWT. Moreover, in accordance with angular momentum conservation, the rotation of ASWT induces a wake opposing its rotational direction. Likewise, owing to the axial length of ASWT, a wake with reverse rotation forms on the unit’s side and wake. The wake generated by the reverse rotation configuration interacts with adjacent units to some extent. Thus, when the parallel spacing is small, the C_P and C_T of the reverse rotation configuration are greater than those of the co-rotation configuration. Figure 6 shows the velocity distribution behind the double units at different x . Regardless of whether the configuration is reverse rotation or co-rotation, as the distance behind increases, the wake of the double units gradually recovers. Moreover, the velocity distribution of the reverse rotation configuration exhibits better symmetry, whereas there are noticeable disparities in the velocity distribution of the co-rotation configuration, particularly as the parallel spacing decreases. This also indirectly corroborates the reason for the significant difference between C_P and C_T in the co-rotation configuration illustrated in Figure 4.

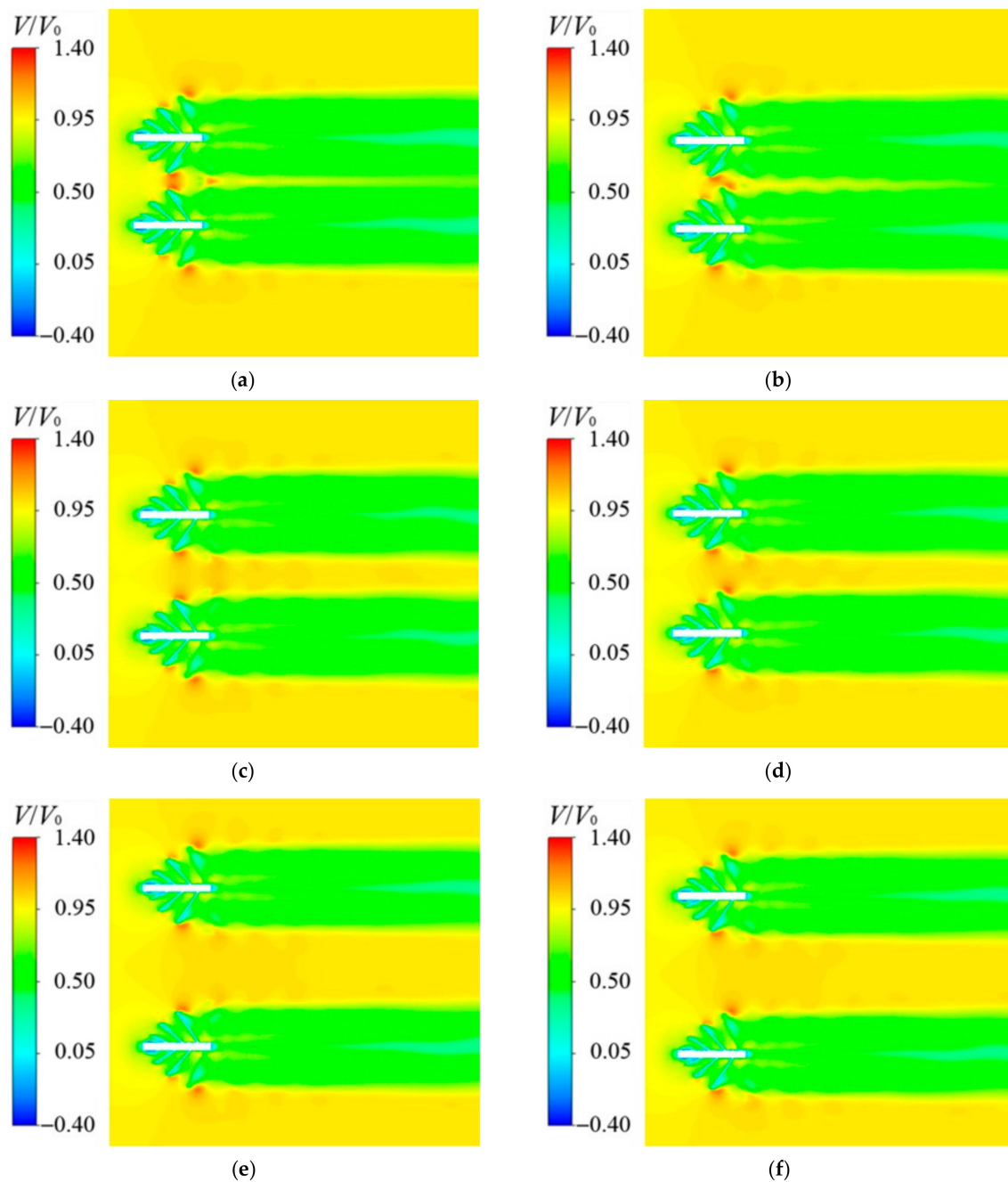


Figure 5. Velocity contours for the double units at different x : (a) $x = 1.1 D$ reverse rotation; (b) $x = 1.1 D$ co-rotation; (c) $x = 1.5 D$ reverse rotation; (d) $x = 1.5 D$ co-rotation; (e) $x = 2.0 D$ reverse rotation; (f) $x = 2.0 D$ co-rotation.

Figure 7 illustrates the three-dimensional vortex structures using the Q-criterion of 0.1 s and colored by the velocity for the double units at different x . Regardless of whether it is a reverse rotation or co-rotation configuration, the vortex structures of the double units will influence each other to some extent. When the parallel spacing is small, in the case of the counter-rotation configuration, the vortex exhibits a gear-like meshing effect, continuing to develop rearward in a long helical pattern [45], resulting in an overall vortex structure that is mirror-symmetrically distributed. In contrast, for the co-rotation configuration, the vortex conflicts and intertwines, forming an asymmetric structure. As the parallel spacing increases, the mutual influence of the wakes gradually weakens, and the vortex structures of both configurations gradually return to a form similar to that of an isolated ASWT.

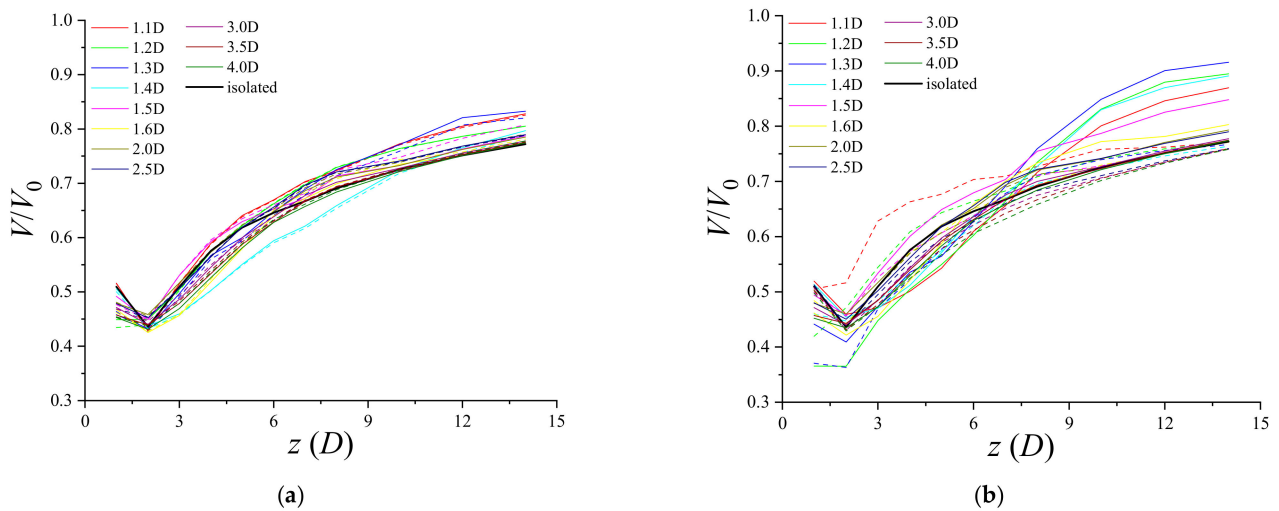


Figure 6. Velocity distribution behind the double units at different x . (The solid and dashed lines of the same color in the figure represent the left and right units, respectively): (a) reverse rotation; (b) co-rotation.

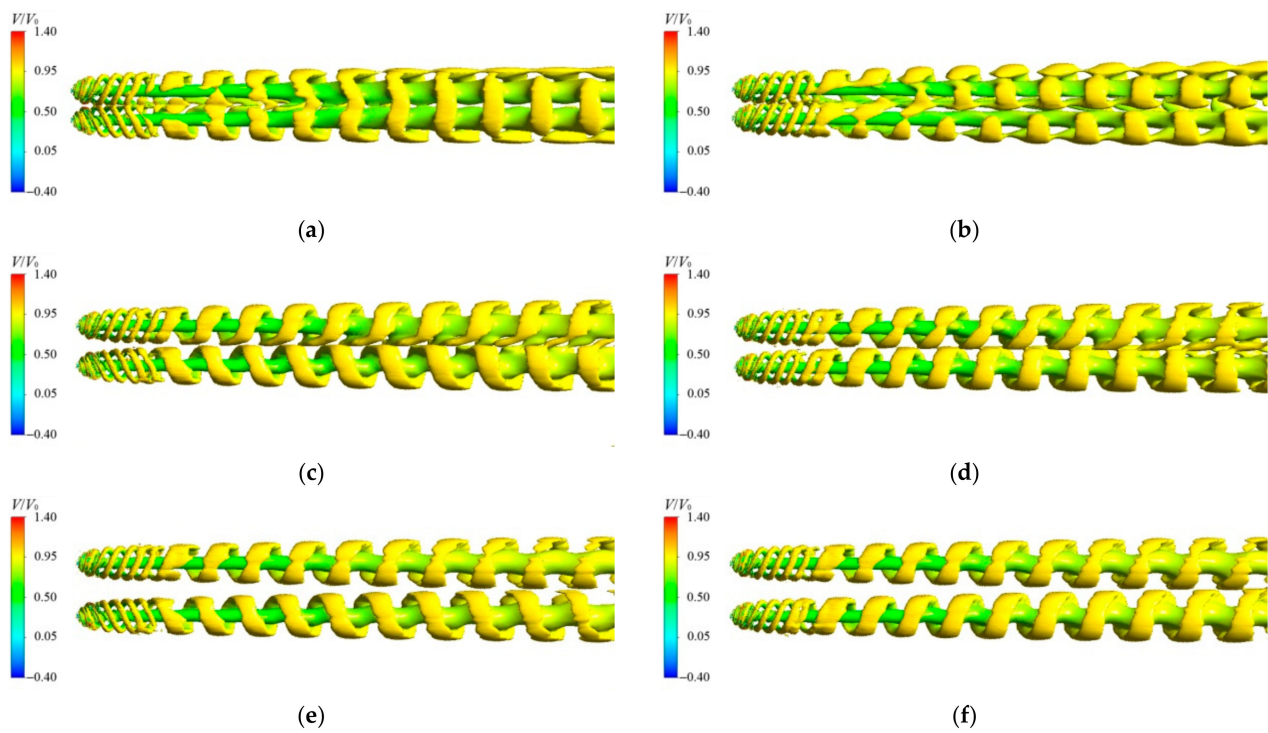


Figure 7. 3D vortex structures colored by velocity for the double units at different x : (a) $x = 1.1$ D reverse rotation; (b) $x = 1.1$ D co-rotation; (c) $x = 1.5$ D reverse rotation; (d) $x = 1.5$ D co-rotation; (e) $x = 2.0$ D reverse rotation; (f) $x = 2.0$ D co-rotation.

3.2. Tandem Arrangement

Figure 8 illustrates the variations in C_P and C_T of tandem arrangement of double units as the tandem spacing (z) changes. For tandem arrangements, whether in reverse or co-rotation configuration, the C_P and C_T of the upstream unit remain nearly consistent with those of the isolated ASWT when the tandem spacing (z) is 5 D, thereafter remaining unaffected by the downstream unit. The C_P and C_T of the downstream unit decrease rapidly under narrow z . Specifically, when the downstream unit is configured for co-rotation and has a tandem spacing of less than 2 D, there may even be cases where both the C_P and C_T are

negative. In such instances, the wake effect of the upstream unit will completely overturn the downstream unit. When $z = 5 D$, the C_P and C_T of the downstream unit in reverse rotation configuration recover to 39.8% and 44.3% of the isolated ASWT, respectively, while those in co-rotation configuration recover to 26.0% and 37.8%, respectively. Subsequently, this increasing trend slows down significantly. By the time z increases to 10 D, the C_P and C_T of the downstream unit in reverse rotation configuration recover to 47.2% and 52.1% of the isolated ASWT, respectively, while those in co-rotation configuration recover to 39.8% and 48.7%, respectively. Comparing the two rotation configurations, although both downstream units experience varying degrees of performance degradation, the recovery of downstream unit performance in the reverse rotation configuration is significantly faster than in the co-rotation configuration. Additionally, it is noteworthy that due to the low tip speed ratio of ASWT operation, the influence of turbulence is relatively small. Compared to lift-type horizontal-axis wind turbines operating at high tip speed ratios, ASWT can form denser serial arrays, thus maximizing the energy density of the array.

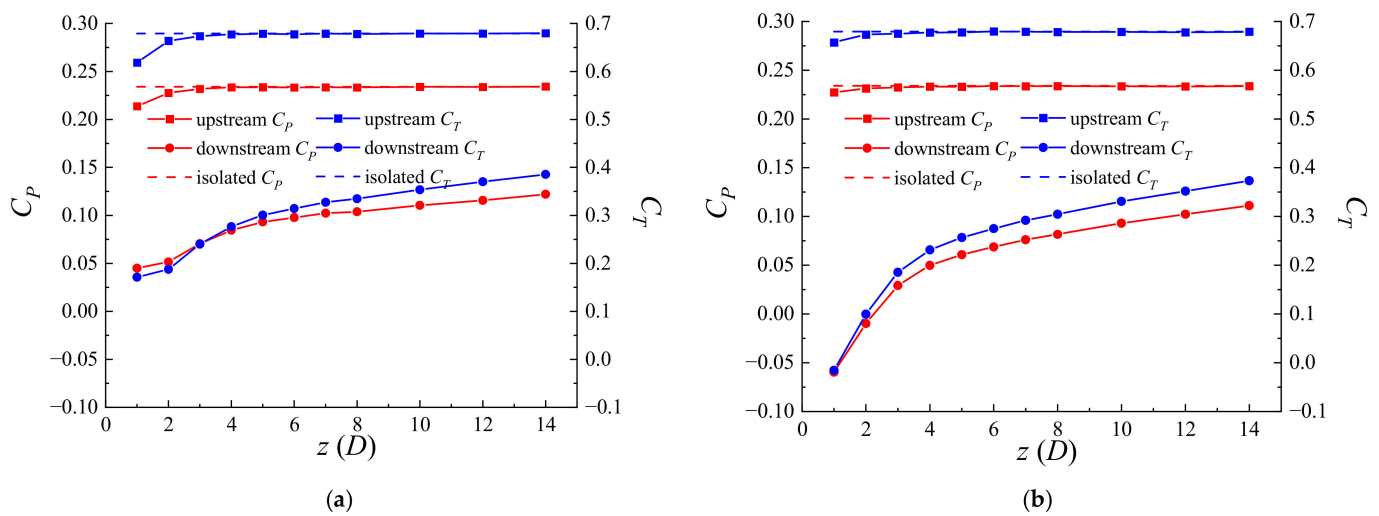


Figure 8. C_P and C_T versus z for the double units: (a) reverse rotation; (b) co-rotation.

Figure 9 shows the velocity distribution behind the upstream unit at different z . When z is less than 5 D, the downstream unit in reverse rotation configuration exhibits a quicker velocity recovery compared to the co-rotation configuration within the near wake region. When z is greater than 5 D, the wake velocity distribution of the upstream unit remains essentially consistent with that of an isolated ASWT, with minimal influence from the downstream unit. Additionally, the wake velocity distribution of the downstream units in both reverse and co-rotation configurations remains largely consistent. Furthermore, to better illustrate the distinctions between the two rotation configurations, Figure 10 shows the velocity streamlines at a position 0.5 D downstream of the downstream unit at different z . Since the downstream unit is fully immersed in the wake of the upstream unit, it absorbs most of the incoming flow energy, resulting in reduced available kinetic energy for the downstream unit. Consequently, its C_P and C_T levels are notably lower than those of the upstream unit. However, the downstream unit in reverse rotation configuration excels in absorbing the residual energy from the upstream, as the downstream flow velocity for reverse rotation configuration is lower than for co-rotation configuration. According to angular momentum conservation, a counter-rotation rotor generates trailing momentum opposite to its rotation. In the reverse rotation configuration, the wake field of the upstream unit exhibits trailing momentum in the same direction as the downstream unit [46,47], which is similar to the results of traditional horizontal-axis turbines. Hence, the downstream unit in reverse rotation configuration acquires more energy compared to that in co-rotation configuration, elucidating why the downstream unit in reverse rotation configuration in Figure 8 exhibits higher C_P and C_T .

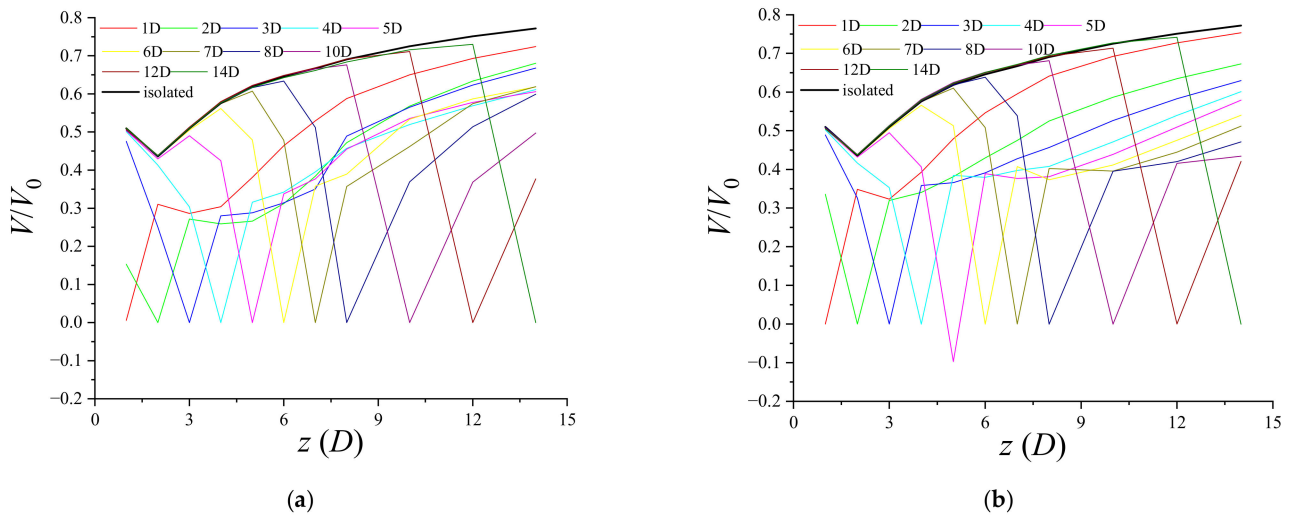


Figure 9. Velocity distribution behind the double units at different z . (The solid and dashed lines of the same color in the figure represent the left and right units, respectively): (a) reverse rotation; (b) co-rotation.

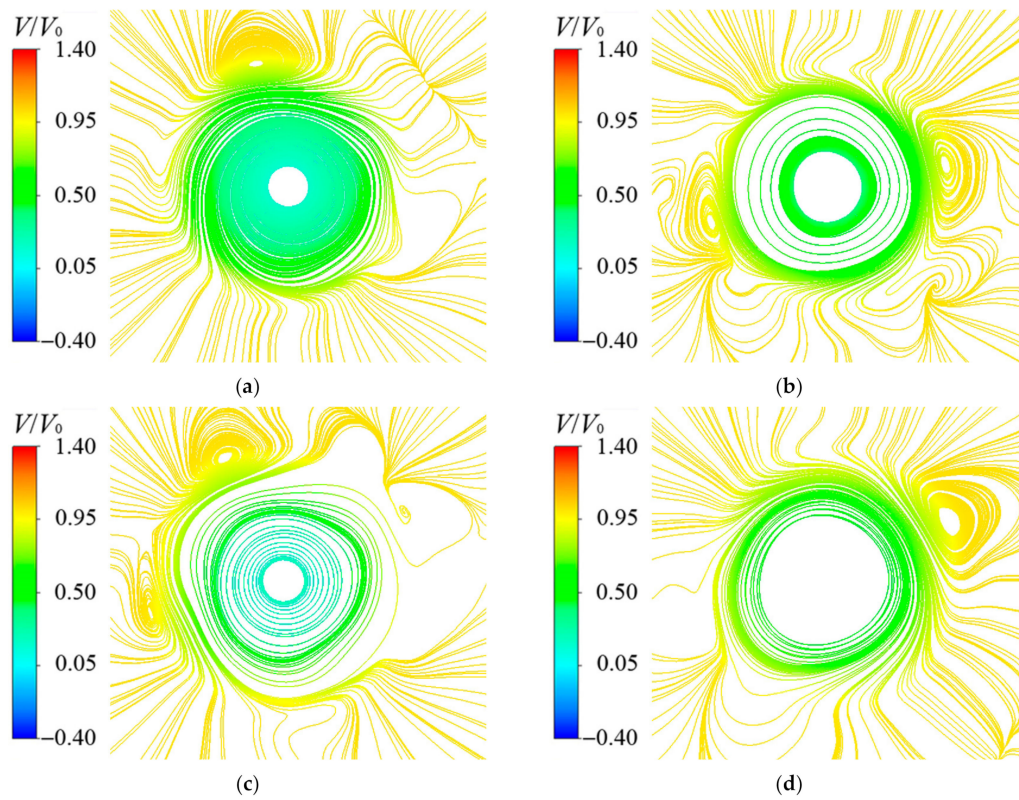


Figure 10. Cont.

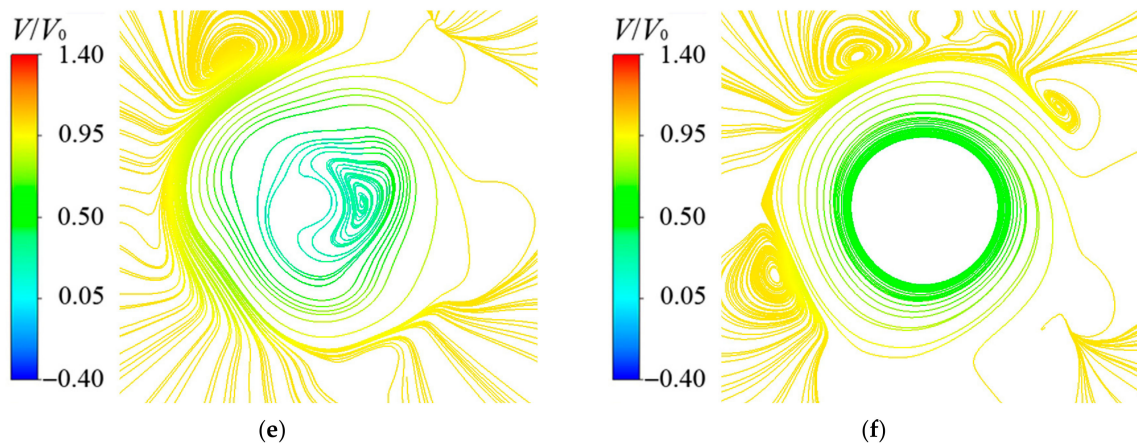


Figure 10. Velocity streamlines at a position 0.5 D downstream of the downstream unit at different z : (a) $z = 3$ D reverse rotation; (b) $z = 3$ D co-rotation; (c) $z = 5$ D reverse rotation; (d) $z = 5$ D co-rotation; (e) $z = 7$ D reverse rotation; (f) $z = 7$ D co-rotation.

Figure 11 illustrates the three-dimensional vortex structures using the Q-criterion of 0.1 s and colored by the velocity for the double units at different z . It is evident that irrespective of whether the double units are in reverse or co-rotation configurations, the vortex near the upstream unit remains unaffected. In the case of the reverse rotation configuration, the vortex near the downstream unit, after superposition, becomes somewhat chaotic, leading to a degree of wake distortion. Conversely, in the co-rotation configuration, the vortex near the downstream unit seamlessly integrates with the upstream vortex, appearing more as an extension and continuation of it.

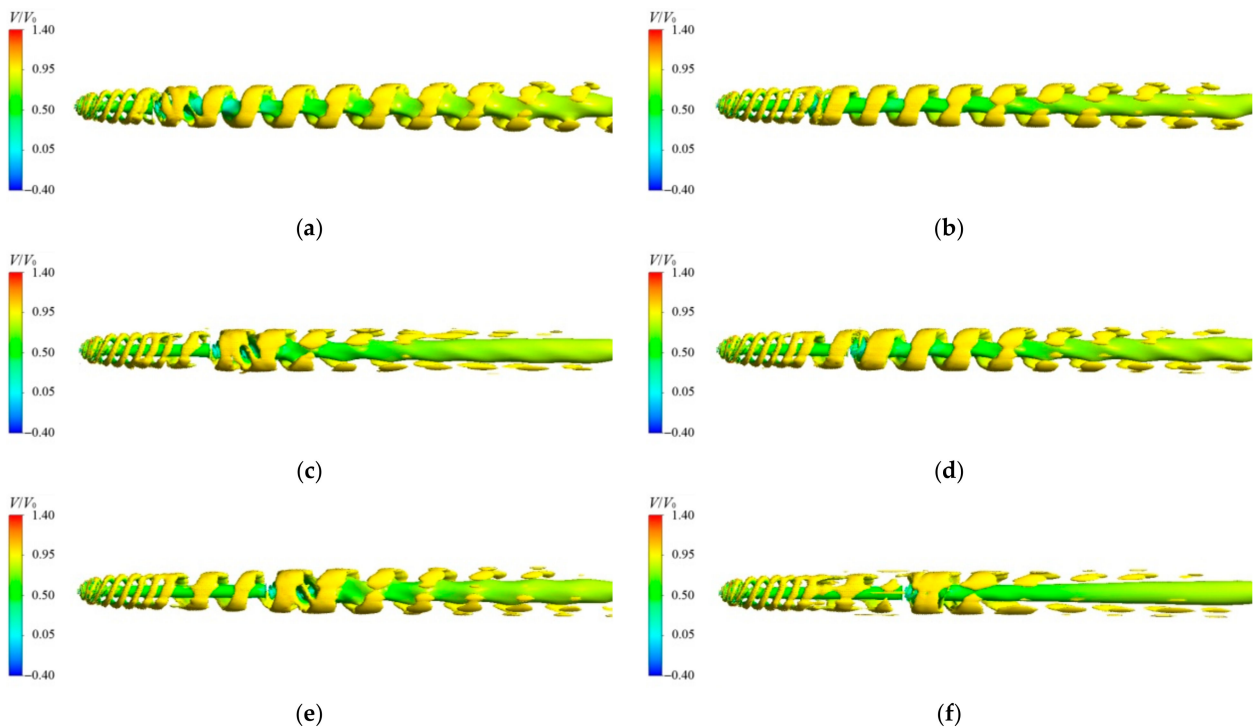


Figure 11. 3D vortex structures colored by velocity for the double units at different z : (a) $z = 3$ D reverse rotation; (b) $z = 3$ D co-rotation; (c) $z = 5$ D reverse rotation; (d) $z = 5$ D co-rotation; (e) $z = 7$ D reverse rotation; (f) $z = 7$ D co-rotation.

3.3. Triangular Array

Through the study of parallel and tandem arrangements, it can be found that the wake effect of the upstream turbine and the blocking effect between adjacent turbines are the main factors that affect the performance of an array of ASWT. To minimize the wake effect from the upstream turbine and enhance the overall performance of the array, an interleaved arrangement can be adopted. This arrangement effectively utilizes the blocking effect between turbines and reduces the impact on the downstream turbines. The focus of this section is to study the coupling gain effect of a triangular array under two different rotation configurations, considering the distance x perpendicular to the flow direction and the distance z parallel to the flow direction, as shown in Figure 12.

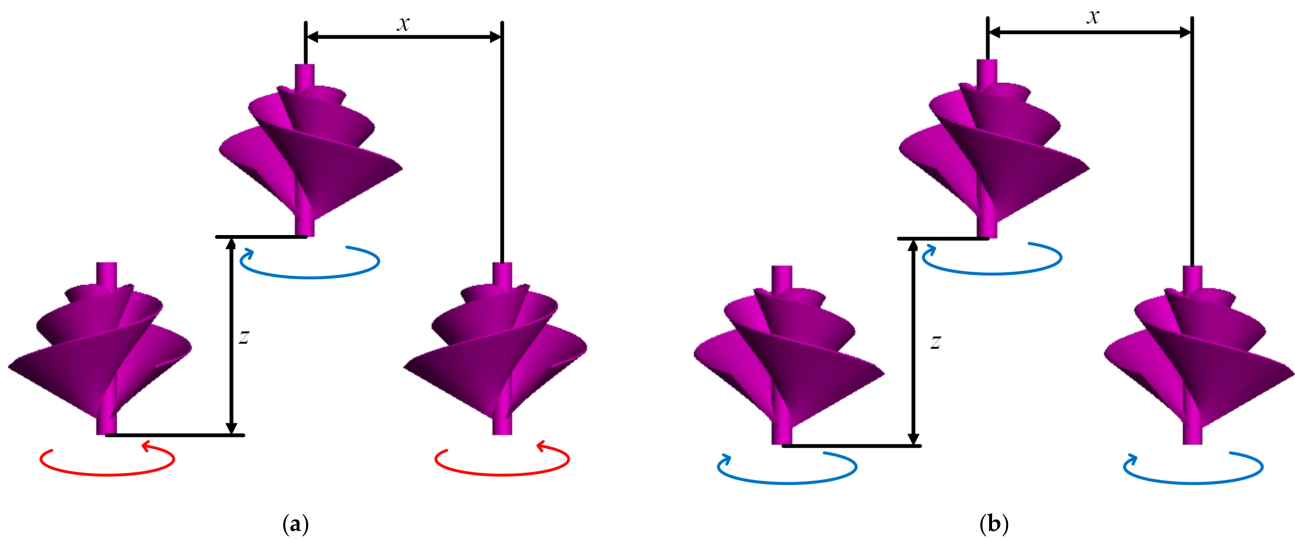


Figure 12. Two rotation schemes for the triangular array: (a) reverse rotation; (b) co-rotation.

To enable a more straightforward comparison of the isolated ASWT and the triangular array, the relative power coefficient change rate ΔC_P is defined as:

$$\Delta C_P = \frac{C_{\bar{P}} - C_{Piso}}{C_{Piso}} \tag{4}$$

where $C_{\bar{P}}$ represents the average C_P of three ASWTs in a triangular array.

The ΔC_P of a triangular array in the reverse rotation and co-rotation configurations are shown in Tables 3 and 4, respectively. For a triangular array, whether in reverse or co-rotation configuration, the downstream turbines experience substantial wake effects when the x between the turbines is less than the turbine diameter (D), resulting in lower $C_{\bar{P}}$ than those of an isolated ASWT. However, when the spacing increases to $x = 1.2 D$, the $C_{\bar{P}}$ values exceed those of an isolated ASWT. As the spacing (x) continues to increase, the $C_{\bar{P}}$ values become higher than those of the isolated ASWT. For the co-rotation configuration, the maximum value is at $x = 1.6 D$ and $z = 1.0 D$, demonstrating a 2.28% increase in the $C_{\bar{P}}$ compared to an isolated ASWT. This maximum value occurs when the wake effect is minimal and there is a strong coupling gain effect between the downstream turbines. For the reverse rotation configuration, the performance mirrors that of turbines with the co-rotation. However, the maximum value emerges at $x = 1.2 D$, with a 2.56% increase in the $C_{\bar{P}}$ compared to an isolated ASWT. Therefore, the reverse rotation configuration resulted in a more pronounced gain effect, suggesting that the downstream turbine could generate a more substantial coupling gain with the upstream turbine’s wake. Additionally, the reverse rotation placement presents distinct advantages, such as higher energy utilization and a more compact arrangement, leading to greater energy density.

Table 3. Triangular array with the reverse rotation configuration.

$x \backslash z$	1.0	1.2	1.4	1.6	1.8	2.0
1.0	−0.01140	−0.00855	−0.00997	−0.01140	−0.00997	−0.00997
1.2	0.011396	0.011396	0.014246	0.014246	0.011396	0.011396
1.4	0.025642	0.019944	0.014246	0.017094	0.014246	0.011396
1.6	0.022792	0.022792	0.019984	0.017350	0.019944	0.017094
1.8	0.023842	0.022792	0.019944	0.019646	0.019944	0.017094
2.0	0.019944	0.019944	0.019760	0.017094	0.019668	0.014246

Table 4. Triangular array with the co-rotation configuration.

$x \backslash z$	1.0	1.2	1.4	1.6	1.8	2.0
1.0	−0.00997	−0.00427	−0.00427	−0.00472	−0.00142	−0.00285
1.2	0.011396	0.014246	0.011396	0.011396	0.005698	0.005698
1.4	0.019944	0.014246	0.020864	0.017094	0.011396	0.011396
1.6	0.022792	0.017094	0.019944	0.019944	0.014246	0.017094
1.8	0.022792	0.019944	0.019944	0.017094	0.017094	0.017094
2.0	0.019944	0.016850	0.017094	0.016850	0.017094	0.016850

$z = 1 \text{ D}$ and $x = 1.4 \text{ D}$ serve as the threshold parameters for achieving a positive coupling effect in the reverse rotation configuration. The turbulence kinetic energy and pressure contours for the triangular array at $z = 1 \text{ D}$, $x = 1 \text{ D}$ and $z = 1 \text{ D}$, $x = 1.4 \text{ D}$ are compared in Figures 13 and 14, respectively. When x is 1 D , part of the downstream ASWT’s frontal area is exposed to the upstream ASWT’s wake, leading to a significant reduction in the high-pressure region in front of the ASWT. However, this does not occur at $x = 1.4 \text{ D}$, where a larger portion of the ASWT’s frontal area benefits from the accelerated wake of the upstream ASWT. This results in a higher performance compared to the isolated ASWT.

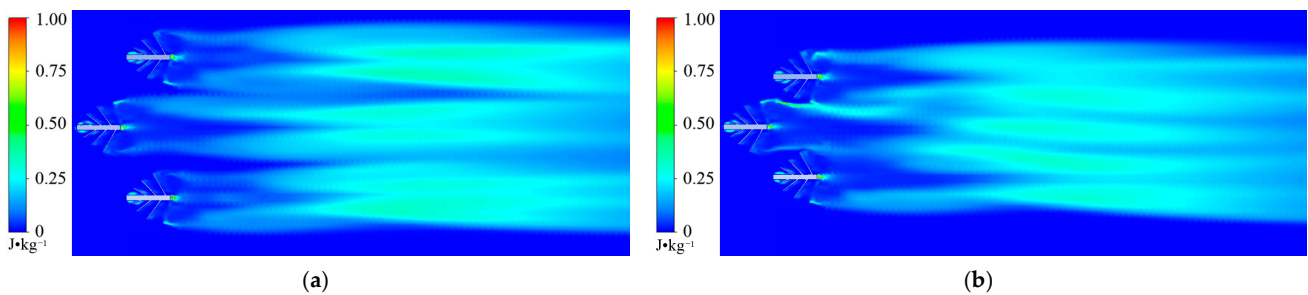


Figure 13. Turbulence kinetic energy contours of triangular arrangement: (a) $z = 1.0 \text{ D}$, $x = 1.4 \text{ D}$; (b) $z = 1.0 \text{ D}$, $x = 1.0 \text{ D}$.

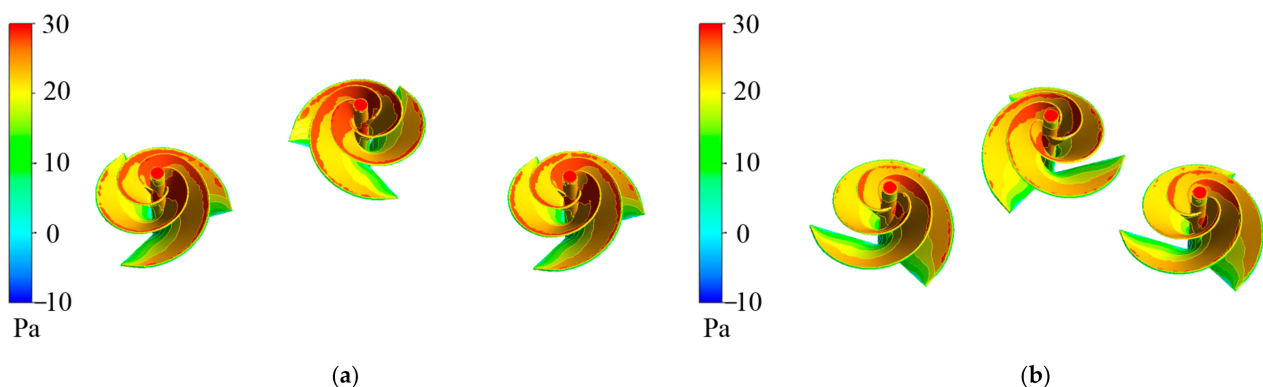


Figure 14. Pressure contours of triangular arrangement: (a) $z = 1.0 \text{ D}$, $x = 1.4 \text{ D}$; (b) $z = 1.0 \text{ D}$, $x = 1.0 \text{ D}$.

4. Conclusions

This study utilizes computational fluid dynamics simulations to thoroughly examine the aerodynamic performance and coupling gain effect for ASWTs in parallel, tandem arrangement, triangular array, and different rotational configurations. The key findings of this research are as follows:

(1) In parallel arrangement, benefiting from the coupling gain effect, both reverse and co-rotation configurations of ASWTs achieve higher performance than an isolated ASWT within a specific range of parallel spacing. The reverse rotation configuration achieves the maximum coupling gain, with the average C_P increased 3.53% compared to the isolated ASWT at a spacing (x) of 1.1 D. As the parallel spacing increases, the C_P and C_T of the double units in both configurations exhibit a continuous decreasing trend, eventually approaching the values of an isolated ASWT.

(2) In tandem arrangement, under the influence of the wake effect, the C_P and C_T of the upstream turbine experience a slight decrease, and those of the downstream turbine decrease rapidly within the spacing (z) of 5 D. The downstream turbine in the reverse rotation configuration acquires more energy compared to the co-rotation configuration, leading to a significantly faster recovery of the performance.

(3) The triangular array can achieve a 2.56% increase in the maximum performance under an optimal configuration, thanks to the coupling gain and wake effect. Additionally, the reverse rotation configuration exhibits a greater energy density due to the meshing effect between the wake of the upstream turbine and the downstream turbine, allowing it to sustain a higher maximum output with smaller spacing between the ASWTs.

Author Contributions: Conceptualization, K.S.; methodology, K.S. and L.W.; software, H.H. and L.W.; validation, H.H.; formal analysis, K.S.; investigation, K.S.; resources, K.S.; data curation, K.S.; writing—original draft preparation, K.S.; writing—review and editing, L.W. and C.L.; visualization, C.L.; supervision, C.L.; project administration, K.S.; funding acquisition, K.S. All authors have read and agreed to the published version of the manuscript.

Funding: This work was supported by the Xingdian Talent Support Program of Yunnan Province (grant no. XDYC-QNRC-2023-0159), the Key Laboratory of Yunnan Advanced Equipment Intelligent Manufacturing Technology (grant no. KLYAEIMTY2022001), and the Yunnan Fundamental Research Project (grant no. 202201AU070028).

Institutional Review Board Statement: Not applicable.

Informed Consent Statement: Not applicable.

Data Availability Statement: Data is contained within the article.

Conflicts of Interest: The authors declare no conflicts of interest.

References

1. Olabi, A.G.; Abdelkareem, M.A. Renewable energy and climate change. *Renew. Sustain. Energy Rev.* **2022**, *158*, 112111. [[CrossRef](#)]
2. Li, L.; Lin, J.; Wu, N.; Xie, S.; Meng, C.; Zheng, Y.; Zhao, Y. Review and outlook on the international renewable energy development. *Energy Built Environ.* **2022**, *3*, 139–157. [[CrossRef](#)]
3. Matsumoto, K.I.; Matsumura, Y. Challenges and economic effects of introducing renewable energy in a remote island: A case study of Tsushima Island, Japan. *Renew. Sustain. Energy Rev.* **2022**, *162*, 112456. [[CrossRef](#)]
4. Ahmed, S.D.; Al-Ismail, F.S.; Shafiullah, M.; Al-Sulaiman, F.A.; El-Amin, I.M. Grid integration challenges of wind energy: A review. *IEEE Access* **2020**, *8*, 10857–10878. [[CrossRef](#)]
5. Summerfield-Ryan, O.; Park, S. The power of wind: The global wind energy industry's successes and failures. *Ecol. Econ.* **2023**, *210*, 107841. [[CrossRef](#)]
6. Porté-Agel, F.; Bastankhah, M.; Shamsoddin, S. Wind-turbine and wind-farm flows: A review. *Bound.-Layer Meteorol.* **2020**, *174*, 1–59. [[CrossRef](#)] [[PubMed](#)]
7. Johari, M.K.; Jalil, M.; Shariff, M.F.M. Comparison of horizontal axis wind turbine (HAWT) and vertical axis wind turbine (VAWT). *Int. J. Eng. Technol.* **2018**, *7*, 74–80. [[CrossRef](#)]
8. Rehman, S.; Alam, M.M.; Alhems, L.M.; Rafique, M.M. Horizontal axis wind turbine blade design methodologies for efficiency enhancement—A review. *Energies* **2018**, *11*, 506. [[CrossRef](#)]

9. Castellanos Bustamante, R.; Roman Messina, A.; Ramirez Gonzalez, M.; Calderon Guizar, G. Assessment of frequency performance by wind integration in a large-scale power system. *Wind Energy* **2018**, *21*, 1359–1371. [[CrossRef](#)]
10. Murali, A.; Rajagopalan, R.G. Numerical simulation of multiple interacting wind turbines on a complex terrain. *J. Wind Eng. Ind. Aerodyn.* **2017**, *162*, 57–72. [[CrossRef](#)]
11. Schallenberg-Rodríguez, J.; Montesdeoca, N.G. Spatial planning to estimate the offshore wind energy potential in coastal regions and islands. Practical case: The Canary Islands. *Energy* **2018**, *15*, 143. [[CrossRef](#)]
12. Abramic, A.; Mendoza, A.G.; Haroun, R. Introducing offshore wind energy in the sea space: Canary Islands case study developed under Maritime Spatial Planning principles. *Renew. Sustain. Energy Rev.* **2021**, *145*, 111119. [[CrossRef](#)]
13. Ji, H.S.; Baek, J.H.; Mieremet, R.; Kim, K.C. The aerodynamic performance study on small wind turbine with 500W class through wind tunnel experiments. *Int. J. Renew. Energy Sources* **2016**, *1*, 7–12.
14. Song, K.; Huan, H.; Kang, Y. Aerodynamic Performance and Wake Characteristics Analysis of Archimedes Spiral Wind Turbine Rotors with Different Blade Angle. *Energies* **2023**, *16*, 385. [[CrossRef](#)]
15. Lu, Q.; Li, Q.; Kim, Y.K.; Kim, K.C. A study on design and aerodynamic characteristics of a spiral-type wind turbine blade. *J. Korean Soc. Vis.* **2012**, *10*, 27–33.
16. Kim, K.C.; Ji, H.S.; Kim, Y.K.; Lu, Q.; Baek, J.H.; Mieremet, R. Experimental and numerical study of the aerodynamic characteristics of an archimedes spiral wind turbine blade. *Energies* **2014**, *7*, 7893–7914. [[CrossRef](#)]
17. Safdari, A.; Kim, K.C. Aerodynamic and structural evaluation of horizontal archimedes spiral wind turbine. *J. Clean Energy Technol.* **2015**, *3*, 34–38. [[CrossRef](#)]
18. Chaudhary, S.; Jaiswal, S.; Nanda, R.; Patel, S.; Kumar, P. Comparison of torque characteristics of Archimedes wind turbine evaluated by analytical and experimental study. *Int. J. Mech. Prod. Eng.* **2016**, *4*, 75–78.
19. Rao, S.S.; Shanmukesh, K.; Naidu, M.K.; Kalla, P. Design and analysis of Archimedes aero-foil wind turbine blade for light and moderate wind speeds. *Int. J. Recent Technol. Mech. Electr. Eng.* **2018**, *5*, 1–5.
20. Jang, H.; Kim, D.; Hwang, Y.; Paek, I.; Kim, S.; Baek, J. Analysis of Archimedes spiral wind turbine performance by simulation and field test. *Energies* **2019**, *12*, 4624. [[CrossRef](#)]
21. Nawar, M.A.; Hameed, H.A.; Ramadan, A.; Attai, Y.A.; Mohamed, M.H. Experimental and numerical investigations of the blade design effect on Archimedes Spiral Wind Turbine performance. *Energy* **2021**, *223*, 120051. [[CrossRef](#)]
22. Kamal, A.M.; Nawar, M.A.; Attai, Y.A.; Mohamed, M.H. Blade design effect on Archimedes Spiral Wind Turbine performance: Experimental and numerical evaluations. *Energy* **2022**, *250*, 123892. [[CrossRef](#)]
23. Kamal, A.M.; Nawar, M.A.; Attai, Y.A.; Mohamed, M.H. Archimedes Spiral Wind Turbine performance study using different aerofoiled blade profiles: Experimental and numerical analyses. *Energy* **2023**, *262*, 125567. [[CrossRef](#)]
24. Al-murshedi, A.S.N. Spiral Wind Turbine Investigations for Various Material Constriction Based on Static and Dynamic Analyses. *J. Adv. Stud. Eng. Sci.* **2023**, *2*, 99–109.
25. Refaie, A.G.; Hameed, H.A.; Nawar, M.A.; Attai, Y.A.; Mohamed, M.H. Qualitative and quantitative assessments of an Archimedes Spiral Wind Turbine performance augmented by A concentrator. *Energy* **2021**, *231*, 121128. [[CrossRef](#)]
26. Refaie, A.G.; Hameed, H.A.; Nawar, M.A.; Attai, Y.A.; Mohamed, M.H. Comparative investigation of the aerodynamic performance for several Shrouded Archimedes Spiral Wind Turbines. *Energy* **2022**, *239*, 122295. [[CrossRef](#)]
27. Vanderwende, B.J.; Kosović, B.; Lundquist, J.K.; Mirocha, J.D. Simulating effects of a wind-turbine array using LES and RANS. *J. Adv. Model. Earth Syst.* **2016**, *8*, 1376–1390. [[CrossRef](#)]
28. Bremseth, J.; Duraisamy, K. Computational analysis of vertical axis wind turbine arrays. *Theor. Comput. Fluid Dyn.* **2016**, *30*, 387–401. [[CrossRef](#)]
29. Tang, H.; Lam, K.M.; Shum, K.M.; Li, Y. Wake effect of a horizontal axis wind turbine on the performance of a downstream turbine. *Energies* **2019**, *12*, 2395. [[CrossRef](#)]
30. Zhang, D.; Guo, P.; Wang, Y.; Hu, Q.; Li, J. Performance analysis of a ductless Archimedes screw turbine array for deep-sea power supply. *Ocean Eng.* **2023**, *288*, 116113. [[CrossRef](#)]
31. Labib, A.M.; AbdelGawad, A.F.; Nasseif, M.M. Effect of aspect ratio on aerodynamic performance of Archimedes spiral wind turbine. *Egypt. Int. J. Eng. Sci. Technol.* **2020**, *32*, 66–72. [[CrossRef](#)]
32. Menter, F.R. Two-equation eddy-viscosity turbulence models for engineering applications. *AIAA J.* **1994**, *32*, 1598–1605. [[CrossRef](#)]
33. Song, K.; Kang, Y. A Numerical Performance Analysis of a Rim-Driven Turbine in Real Flow Conditions. *J. Mar. Sci. Eng.* **2022**, *10*, 1185. [[CrossRef](#)]
34. Song, K.; Yang, B. A Comparative Study on the Hydrodynamic-Energy Loss Characteristics between a Ducted Turbine and a Shaftless Ducted Turbine. *J. Mar. Sci. Eng.* **2021**, *9*, 930. [[CrossRef](#)]
35. Lawson, M.J.; Li, Y.; Sale, D.C. Development and verification of a computational fluid dynamics model of a horizontal-axis tidal current turbine. In Proceedings of the ASME 2011 30th International Conference on Ocean, Offshore and Arctic Engineering, Rotterdam, The Netherlands, 19–24 June 2011; pp. 711–720.
36. Moshfeghi, M.; Shams, S.; Hur, N. Aerodynamic performance enhancement analysis of horizontal axis wind turbines using a passive flow control method via split blade. *J. Wind Eng. Ind. Aerodyn.* **2017**, *167*, 148–159. [[CrossRef](#)]
37. Al-Dabbagh, M.A.; Yuce, M.I. Numerical evaluation of helical hydrokinetic turbines with different solidities under different flow conditions. *Int. J. Environ. Sci. Technol.* **2019**, *16*, 4001–4012. [[CrossRef](#)]

38. Ramana Murthy, S.V.; Kishore Kumar, S. Effect of different turbulence models on the numerical analysis of axial flow turbine stage of a typical turbofan engine. In Proceedings of the ASME 2013 Gas Turbine India Conference, Bangalore, Karnataka, India, 5–6 December 2013.
39. Moshfeghi, M.; Song, Y.J.; Xie, Y.H. Effects of near-wall grid spacing on SST-K- ω model using NREL Phase VI horizontal axis wind turbine. *J. Wind Eng. Ind. Aerodyn.* **2012**, *107*, 94–105. [[CrossRef](#)]
40. Ghasemian, M.; Nejat, A. Aerodynamic noise prediction of a horizontal axis wind turbine using improved delayed detached eddy simulation and acoustic analogy. *Energy Convers. Manag.* **2015**, *99*, 210–220. [[CrossRef](#)]
41. Monatrakul, W.; Suntivarakorn, R. Effect of blade angle on turbine efficiency of a Spiral Horizontal Axis Hydro Turbine. *Energy Procedia* **2017**, *138*, 811–816. [[CrossRef](#)]
42. Talukdar, P.K.; Sardar, A.; Kulkarni, V.; Saha, U.K. Parametric analysis of model Savonius hydrokinetic turbines through experimental and computational investigations. *Energy Convers. Manag.* **2018**, *158*, 36–49. [[CrossRef](#)]
43. Apsley, D.D.; Stallard, T.; Stansby, P.K. Actuator-line CFD modelling of tidal-stream turbines in arrays. *J. Ocean Eng. Mar. Energy* **2018**, *4*, 259–271.
44. Ouro, P.; Ramírez, L.; Harrold, M. Analysis of array spacing on tidal stream turbine farm performance using Large-Eddy Simulation. *J. Fluids Struct.* **2019**, *91*, 102732.
45. Song, K.; Huan, H.T.; Wei, L.C.; Liu, C.X. A comparative study of hydrodynamic performance between ducted and non-ducted Archimedes spiral hydrokinetic turbines. *Ocean Eng.* **2024**, *306*, 118087.
46. Allah, V.A.; Mayam, M.H.S. Large Eddy Simulation of flow around a single and two in-line horizontal-axis wind turbines. *Energy* **2017**, *121*, 533–544. [[CrossRef](#)]
47. Veisi, A.A.; Mayam, M.H.S. Effects of blade rotation direction in the wake region of two in-line turbines using Large Eddy Simulation. *Appl. Energy* **2017**, *197*, 375–392. [[CrossRef](#)]

Disclaimer/Publisher’s Note: The statements, opinions and data contained in all publications are solely those of the individual author(s) and contributor(s) and not of MDPI and/or the editor(s). MDPI and/or the editor(s) disclaim responsibility for any injury to people or property resulting from any ideas, methods, instructions or products referred to in the content.